Eco-Evolutionary Dynamics of Proliferation Heterogeneity: A Phenotype-Structured Model for Tumor Growth and Treatment Response

Lara Schmalenstroer [1], Russell C. Rockne [2], Farnoush Farahpour [1,3*]

[1]Bioinformatics and Computational Biophysics, University of Duisburg-Essen, Germany.
[2]Division of Mathematical Oncology and Computational Systems Biology, Beckman Research Institute, City of Hope National Medical Center, California, USA.
[3]Institute for Cell Biology (Cancer Research), University Hospital Essen, Germany.

*Corresponding author(s). E-mail(s): farnoush.farahpour@uni-due.de;
Contributing authors: lara.schmalenstroer@uni-due.de; rrockne@coh.org;

Abstract

Intra-tumor heterogeneity in proliferation rates fundamentally influences cancer progression and treatment resistance. To investigate how continuous phenotypic variation shapes eco-evolutionary dynamics, we develop a phenotype-structured partial differential equation framework that explicitly models proliferation heterogeneity as a dynamic trait distribution. Our model integrates three key biological principles: (1) phenotypic diffusion capturing heritable variation in proliferation rates, (2) global resource competition enforcing density-dependent growth constraints, and (3) an experimentally grounded life-history trade-off linking elevated proliferation to increased mortality. Using adaptive dynamics, we derive the optimum proliferation rate in a growing tumor, showing that the optimal phenotype dynamically shifts toward slower proliferation as tumors approach carrying capacity. We perform *in silico* treatment simulations for four different treatment regimes (pan-proliferation, low-, mid-, and high-proliferation targeting) to show how therapeutic selective pressures reshape fitness landscapes. While all treatments slow down tumor growth, they induce divergent evolutionary trajectories: low- and mid-proliferation targeting enrich fast-proliferating clones,

whereas high-proliferation targeting selects for slower phenotypes. We connect these dynamics with changes in mean proliferation rates during and after treatment. We use adaptive dynamics to explain the shifts in mean proliferation rate during treatment, showing how each regimen alters the maximum fitness proliferation rate. Our work establishes a predictive, evolutionarily grounded framework for understanding how therapy reshapes tumor proliferation landscapes, offering a mechanistic basis for designing strategies that anticipate and counteract adaptive resistance.

Keywords: intra-tumor heterogeneity, proliferation heterogeneity, phenotype-structured PDE, evolutionary dynamics

1 Introduction

Biological populations are inherently heterogeneous. Even genetically related individuals can differ substantially in phenotypic traits such as reproduction rate (Travers et al. 2015), metabolic activity (Zhang et al. 2025), and stress tolerance (King et al. 2004). This diversity arises through genetic recombination, epigenetic plasticity (Richards 2006), and stochastic gene expression (Raj and van Oudenaarden 2008), thereby creating complex evolutionary landscapes where selection, mutation, and environmental pressures drive dynamic adaptation (de Visser and Krug 2014). Crucially, phenotypic heterogeneity and variation operate within fundamental biophysical constraints: organisms cannot optimize all phenotypic traits simultaneously due to finite energetic resources (Shoval et al. 2012). These universal fitness trade-offs (Stearns 1989) manifest across biological scales. For example, in animals, rapid reproduction often comes at the cost of reduced longevity (Ghalambor and Martin 2001; Partridge et al. 2005; Travers et al. 2015; Lemaître et al. 2015), while in microbes, slow growth frequently enhances stress resistance (King et al. 2004; Lu et al. 2009; Zakrzewska et al. 2011; Phan and Ferenci 2013). More recently, human cell studies have shown that genomic variants favoring proliferation can decrease survival under anticancer therapies (Kim et al. 2024), demonstrating how these principles extend to pathological contexts. Analogous compromises govern immune function (McDade et al. 2016; Schwenke et al. 2016), metabolic specialization (Ganeshan et al. 2019; Ekkers et al. 2022), and drug tolerance (Wood and Cluzel 2012; Schlatter and Kinkel 2015; Herren and Baym 2022).

In cancer, these universal biological principles manifest as intra-tumor heterogeneity (ITH) (Heppner 1984), which represents a fundamental driver of disease progression (Caswell and Swanton 2017) and therapeutic resistance (Maley et al. 2017; Marusyk et al. 2020; Vitale et al. 2021), and can also influence metastasis (Sobral et al. 2022). Within a single tumor mass, cancer cells exhibit marked variability in their traits, including proliferative (Lucas et al. 2025) and metabolic capacity (Meng et al. 2024; Kondo et al. 2021), and treatment sensitivity (Marusyk et al. 2020). This diversity creates complex evolutionary landscapes where subpopulations compete and adapt under selective pressures. Central to this variability is the dynamic heterogeneity in cellular proliferative capacity, a key determinant of tumor growth kinetics and fitness,

that facilitates the exploration of alternative adaptive strategies by tumor cells under distinct conditions, such as untreated expansion or therapeutic stress, each of which may selectively favor specific proliferative ranges.

Various mathematical approaches have been used to model proliferation heterogeneity in cancer. Compartmental ordinary differential equations (ODE) model discretize populations into subpopulations with distinct proliferative capacities, allowing for mechanistic investigation of selection, treatment response, and clonal competition under therapy (Raatz et al. 2021). Agent-based models (ABMs) (Macal and North 2005) excel at simulating emergent spatial and phenotypic heterogeneity through stochastic cell-level behaviors (Farahpour et al. 2018) and are widely used in computational oncology (West et al. 2023). In particular, ABMs have been employed to investigate evolutionary trade-offs between proliferation and migration rates (Gallaher et al. 2019) as well as proliferation rate and treatment resistance (Gatenby et al. 2020) and their role in shaping phenotypic evolution. Stochastic formulations provide complementary approaches for representing proliferation rate heterogeneity through probabilistic dynamics (Raatz et al. 2021; Durrett et al. 2011; Wang et al. 2023). Adaptive dynamics provides a theoretical framework for modeling long-term evolution under frequency-dependent selection. Foundational models in the field have investigated the evolutionary trajectories of systems characterized by continuous adaptive traits, such as proliferation, migration or therapy resistance, explicitly coupling ecological interactions with evolutionary change, emphasizing the critical role of life-history trade-offs. (Brännström et al. 2013; Dieckmann and Law 1996). Finally, phenotype-structured PDE frameworks enable the continuous tracking of evolving trait distributions at the population level. Such trait-structured models have been employed to investigate phenotypic characteristics, including cell motility (Fiandaca et al. 2022) and drug resistance (Lorenzi et al. 2016; Cho and Levy 2018). However, to the best of our knowledge, the proliferation rate has not yet been formulated as an explicit evolving phenotypic trait within this framework.

To investigate the direct impact of evolving proliferative capacity, we formulate a proliferation-structured PDE framework that integrates intra-tumor heterogeneity with a classical tumor growth model while enabling evolutionary analysis. By treating proliferation as a continuously evolving phenotypic trait rather than a fixed parameter, our model provides a mechanistic description of how heterogeneity in growth contributes to macroscopic tumor dynamics. This formulation allows us to relax the conventional assumption of a fixed growth rate, whether at the level of the entire population or of individual subpopulations, and to assess its consequences within a structure that remains directly comparable to fundamental population growth models.

Our model integrates three components critical for tumor growth modeling: (1) Phenotypic diffusion captures stochastic heritable variation driving ITH, a fundamental feature of cancer progression and therapeutic resistance; (2) Global resource competition models systemic nutrient limitations observed in solid tumors, where total tumor burden constrains growth uniformly across all phenotypes; and (3) Explicit life-history trade-offs quantify the fitness cost of proliferation strategies observed in oncology. Within our PDE framework, validation against longitudinal tumor volume

data demonstrates that the life-history trade-off is essential for accurate growth heterogeneity modeling, preventing unrealistic inflation of mean proliferation rates. Through *in silico* treatment experiments, we further show how targeting distinct regions of the proliferation spectrum drives divergent evolutionary trajectories. Using principles from adaptive dynamics (Brännström et al. 2013), we derive the maximum fitness strategy for proliferation rates under resource competition and show how this maximum dynamically shifts during tumor progression, revealing how tumors restructure phenotypic landscapes during growth and treatment response. By unifying concepts from ecology and cancer biology, this work establishes a predictive platform for probing treatment-induced selection and resistance evolution.

2 Materials and Methods

2.1 Data

To calibrate and validate our model, we used longitudinal tumor volume measurements from an untreated group of immunodeficient tumor-bearing mice reported in Zhao et al. (2020) comprising tumor growth trajectories of 11 replicates over 58 days post-implantation. To account for measurement errors due to caliper use, we smoothed the data using 1D splines with the `Dierckx v0.5.4` (Dierckx 2023) package in `Julia v1.12.0` (Bezanson et al. 2017) to ensure smooth and consistent tumor growth trajectories (see Section S1).

2.2 Model Structure

We introduce a phenomenological phenotype-structured PDE model to describe heterogeneous tumor growth with continuous variability in cellular proliferative capacity. The model resolves tumor cell populations in time t and in a continuous phenotypic trait ρ, which represents the intrinsic proliferation rate of individual cells. Two coupled population densities are considered: viable/proliferative cancer cells ($C_v(t,\rho)$) and doomed cells ($C_d(t,\rho)$). For each time point t, the functions C_v and C_d quantify how cells are distributed across the phenotypic axis ρ, thereby capturing intra-tumoral heterogeneity in proliferation rates. Proliferation occurs exclusively in viable cells and follows logistic growth kinetics to capture density-dependent resource limitations, while doomed cells undergo no division and will eventually be cleared from the system. We impose a life-history trade-off where elevated proliferation rates correlate with reduced cellular longevity due to resource allocation conflicts. Stochastic variation in the heritable phenotypic trait is modeled as diffusion across the proliferation rate spectrum.

The phenotypic dynamics governing ITH in proliferation rates are quantified by a coupled PDE system (Equations 1a-d):

$$\frac{\partial C_v(t,\rho)}{\partial t} = \underbrace{D\,\frac{\partial^2 C_v(t,\rho)}{\partial \rho^2}}_{\text{Diffusion}} + \underbrace{\rho\, C_v(t,\rho)\,(1-\frac{N_{total}(t)}{K})}_{\text{Logistic growth}} - \underbrace{k_d\,\rho^s\, C_v(t,\rho)}_{\text{Intrinsic death}} \tag{1a}$$

$$\frac{\partial C_d(t,\rho)}{\partial t} = k_d\,\rho^s\,C_v(t,\rho) - \underbrace{k_{cl}\,C_d(t,\rho)}_{\text{Clearance}} \tag{1b}$$

$$N_v(t) = \int_0^\infty C_v(t,\rho)\,d\rho \tag{1c}$$

$$N_d(t) = \int_0^\infty C_d(t,\rho)\,d\rho \tag{1d}$$

$$N_{total}(t) = N_v(t) + N_d(t) \tag{1e}$$

$$\bar{\rho}(t) = \frac{\int_0^\infty \rho\,C_v(t,\rho)\,d\rho}{N(t)} \tag{1f}$$

Equation (1a) describes the dynamics of viable cancer cells $C_v(t,\rho)$, incorporating three fundamental processes: (1) The diffusion term $D\,\frac{\partial^2 C_v(t,\rho)}{\partial \rho^2}$ formalizes stochastic heritable variation in proliferation phenotypes, capturing genetic and epigenetic instability, driven for example by replication errors, epigenetic fluctuations, or unbiased mutations in regulatory genes. This density-independent formulation models unbiased phenotypic exploration without implying spatial movement. (2) The logistic growth term $\rho\,C_v(t,\rho)\left(1-\frac{N_{total}(t)}{K}\right)$ models resource-limited proliferation, where K denotes the environment's carrying capacity and $N_{total}(t)$ is the total tumor volume. The density-dependent regulation is assumed to depend on the total tumor burden, leading to a nonlocal uniform coupling across phenotype space. This formulation enforces global competition for shared resources while preserving phenotype-specific intrinsic fitness differences. Consequently, density dependence controls ecological saturation through global regulation rather than phenotype-specific competitive coefficients. This is biologically plausible in the absence of mechanisms linking proliferation rate to resource specialization or spatial niche segregation. (3) The death term $d(\rho)C_v(t,\rho)$ models irreversible transitions from viable to doomed state. We implement a life-history trade-offs, with k_d scaling mortality intensity and $s > 0$ determining the shape of proliferation-dependent penalty. This trade-off reflects increased mortality risks for highly proliferative phenotypes due to mechanisms like metabolic exhaustion and DNA damage accumulation (Aktipis et al. 2013; Boddy et al. 2018). Without a life-history trade-off, the combination of phenotypic diffusion and proliferation-driven growth would lead to a systematic drift toward higher population-wide proliferation rates $\bar{\rho}_{total}$ and unrealistic tumor growth. The trade-off term serves as a stabilizing mechanism, ensuring biologically plausible evolutionary dynamics by counterbalancing the fitness advantage of fast proliferation. More detailed information, including the derivations of the mean proliferation rate dynamics, are provided in the supplementary materials (see Section S2).

Equation (1b) describes doomed cell dynamics $C_d(t,\rho)$, where the source term $k_d\rho^s C_v(t,\rho)$ couples C_d to the population of viable cells by quantifying transitions from viable to doomed phenotypic states. Accumulation occurs proportionally to viable cell death rates, with clearance governed by $k_{cl}\,C_d(t,\rho)$. Doomed cells retain the proliferation label inherited at transition but do not proliferate or undergo further phenotypic variation.

Integrating the compartments of viable (C_v) and doomed (C_d) cells across the proliferation rate spectrum yields the volume of the viable and doomed compartments ($N_v(t)$ and $N_d(t)$), respectively (Equations (1c), (1d)). The total tumor volume is calculated as the sum of the viable and doomed volumes (Equations (1e)). This global metric quantifies tumor progression by linking phenotypic heterogeneity to macroscopic tumor size.

The population-wide mean proliferation rate $\bar{\rho}(t)$ (Equation (1f)) is defined as the first moment of the viable cell proliferation rate distribution $\int \rho\, C_v(t,\rho)\, d\rho$, normalized by total tumor volume $N(t)$, quantifying the tumor's effective proliferative capacity per total tumor burden.

2.3 Initial and Boundary Conditions

For computational implementation, the proliferation rate domain is truncated to $\rho \in [0.0, \rho_{\max}]$ where $\rho_{\max}$ is chosen such that $\rho_{\max} \gg \bar{\rho}(t) + 3\sigma(t)$ at all times to ensure that boundary conditions don't influence the solution. Homogeneous Neumann (zero-flux) boundary conditions are imposed at both ends of the domain:

$$\left.\frac{\partial C_v}{\partial \rho}\right|_{\rho=0} = \left.\frac{\partial C_v}{\partial \rho}\right|_{\rho=\rho_{\max}} = 0,$$

enforcing phenotypic conservation by preventing net gain or loss of cells through the boundaries.

The initial condition for viable cancer cells $C_v(t,\rho)$ is set as a normalized Gaussian distribution in proliferation rate space:

$$C_v(0,\rho) = \frac{N_0}{\sqrt{2\,\pi\,\sigma_0^2}}\, e^{-\frac{(\rho-\bar{\rho}_0)^2}{2\,\sigma_0^2}},$$

where N_0 is the initial tumor volume, $\bar{\rho}_0$ is the initial mean proliferation rate and σ_0 is the initial standard deviation. Given the small initial tumor volume, we assume no doomed cells are present at $t = 0$:

$$C_d(0,\rho) = 0 \quad \text{for all } \rho.$$

2.4 Parameter Calibration

Model parameters were calibrated using longitudinal tumor volume data. The diffusion coefficient D, the initial standard deviation σ_0, the parameters governing the proliferation-mortality trade-off (k_d and s), and the clearance rate for doomed cells k_{cl} were fitted to replicate-level tumor growth trajectories in the PDE framework. The carrying capacity K was individually calibrated per tumor replicate using an ODE-based logistic model to simplify PDE parameter estimation. Finally, the initial mean proliferation rate $\bar{\rho}_0$ was inferred via hierarchical Bayesian modeling across all 11 replicates' growth trajectories.

The simulation timeframe corresponds precisely to the experimental observation window (58 days), ensuring direct comparability with measured tumor dynamics.

2.5 Implementation and Simulation

All modeling and simulation workflows were performed in `Julia v1.12.0`. The partial differential equation system (Equations 1a-d) was implemented and discretized using `ModelingToolkit v10.26.0` (Ma et al. 2022) and `MethodOfLines v0.11.9` (MoL 2026) and solved using `OrdinaryDiffEq v.6.102.0` (Rackauckas and Nie 2017). Post-processing and visualization of time-resolved phenotype distributions, tumor volumes and mean proliferation rates were performed programmatically within the Julia ecosystem.

3 Results

Replicate-specific parameterization of the heterogeneous growth model

The PDE model (Equations 1a-f) was fitted to longitudinal tumor volume measurements from 11 tumor replicates (see Section 2.1) through optimization of parameters k_d, s, k_{cl}, D, and σ_0 for each replicate. Carrying capacity K was individually calibrated per tumor replicate using an ODE-based logistic model to simplify PDE parameter estimation.

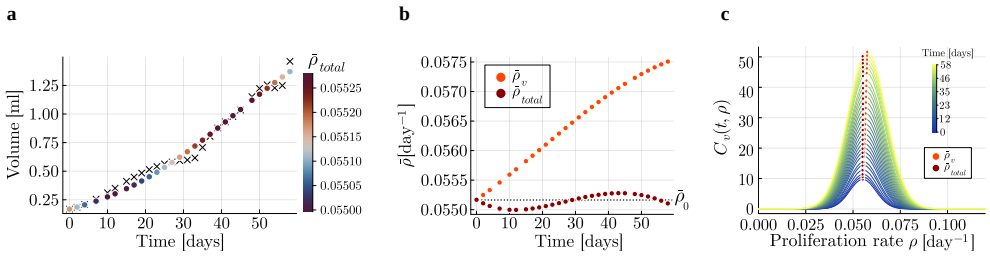

Fig. 1 Model validation and phenotypic dynamics for tumor replicate 174 **(a)** Tumor volume trajectories: PDE solutions (colored dots, hue scaled by population-wide mean proliferation rate $\bar{\rho}_{total}$) versus experimental measurements (black crosses). **(b)** Proliferation rate evolution: Temporal dynamics of $\bar{\rho}_{total}$ (entire population, red) and $\bar{\rho}_v$ (viable subpopulation, orange). Black dotted line indicates initial $\bar{\rho}_{total}(0) = 0.05516$ [day^{-1}]. **(c)** Phenotypic restructuring: Viable cell distributions $C_v(t, \rho)$ from $t_0 = 0$ days (dark blue) to $t_{end} = 58$ days (yellow). Red and orange dots mark $\bar{\rho}_{total}(t)$ and $\bar{\rho}_v(t)$ at sampled time points. Parameters $D = 4.87e-7$ [day^{-3}], $\sigma_0 = 0.0065$ [day^{-1}], $s = 3.96$, $k_d = 97.76$ [day^{s-1}], and $k_{cl} = 0.001$ [day^{-1}] were fitted; carrying capacity $K = 1.97$ [ml] was replicate-specific.

The model solutions are visualized for replicate 174 (Figure 1). The predicted growth trajectories show close agreement with the experimental measurements (Figure 1a). The model accurately captured the logistic growth pattern, while simultaneously resolving the underlying phenotypic evolution. Fits for the remaining replicates are provided in the supplementary material (see Section S4).

Temporal patterns in the population-wide mean proliferation rate $\bar{\rho}_{total}$ (color-coded) were observed across the experimental period, with detailed dynamics illustrated in Figure 1b. The mean proliferation rate of the entire population $\bar{\rho}_{total}$ exhibited fluctuations around the initial value, with an early decline, a peak around day 45, and a decrease toward the end of the observation period (red dots). In contrast, the proliferation rate of the viable subpopulation $\bar{\rho}_v$ steadily increased over time (orange dots)

A continuous restructuring of the population composition occurred throughout tumor progression, as visualized in Figure 1c. The initial Gaussian profile (dark blue) increased in amplitude, representing an increase in tumor volume, and broadened progressively due to diffusion-driven phenotypic variation. Crucially, the proliferation rate $\bar{\rho}_{total}$ (red dots) systematically resided leftward of the viable distribution's peaks (with the orange dots representing the mean proliferation rate of the viable population, $\bar{\rho}_v$) throughout tumor progression.

The fluctuations in the mean proliferation rates $\bar{\rho}_{total}$ and $\bar{\rho}_v$ arise from multiple processes: Phenotypic diffusion continuously introduces both slow- and fast-proliferating cells, while faster-proliferating phenotypes intrinsically dominate population growth, increasing both $\bar{\rho}_{total}$ and $\bar{\rho}_v$. Conversely, the trade-off mortality selectively eliminates cells with high proliferation rates, introducing doomed cancer cells without proliferative capacity into the system, reducing both $\bar{\rho}_{total}$ and $\bar{\rho}_v$. The clearance rate k_{cl} further modulates this effect by determining the retention time of doomed cells. These mechanisms explain why the most abundant phenotype (distribution peaks) does not align with population-averaged proliferation rates $\bar{\rho}_{total}$ but with the viable population's mean proliferation rate $\bar{\rho}_v$. Towards the end of the experimental observation window the mean proliferation rates $\bar{\rho}_{total}$ is decreasing. This behavior can be explained by the mircoenvironment-driven adaptive shift towards slower proliferation predicted by the maximum fitness strategy as the tumor approaches carrying capacity (see Section 3).

By incorporating heterogeneous proliferation rates into the growth model, our model predicts tumor growth with a dynamically changing tumor composition. This approach significantly enhances our ability to model the evolution of tumor growth and the emergence of sub-populations under different selective pressures (see Section 3.

Asymptotic behavior of the model

To characterize the model's long-term behavior, we simulated the model for 2000 days for a tumor using the fitted parameters from the previous section. We simulated the model for a tumor with the parameters $K = 1.05$ [ml] $s = 1.371$, $k_d = 0.74$ [day$^{(1-s)}$], $k_{cl} = 0.001$ [day^{-1}], $D = 4.87e-7$ [day^{-3}], $\sigma_0 = 0.00662$ [day^{-1}]. The total tumor volume $N_{total}(t)$ initially grows toward carrying capacity but then stabilizes slightly below K (Figure 2a). The total tumor volume consists of the volumes of viable cells N_v and doomed cells N_d. During tumor growth, the viable subpopulation grows (orange curve in Figure 2b), followed by a volume reduction after reaching carrying capacity and an increase in the doomed subpopulation curve in Figure 2b), indicating necrosis.

This phenotypic restructuring is evident in the evolving viable cell distribution $C_v(t, \rho)$ (Figure 2c): the initial normal distribution centered around the initial mean

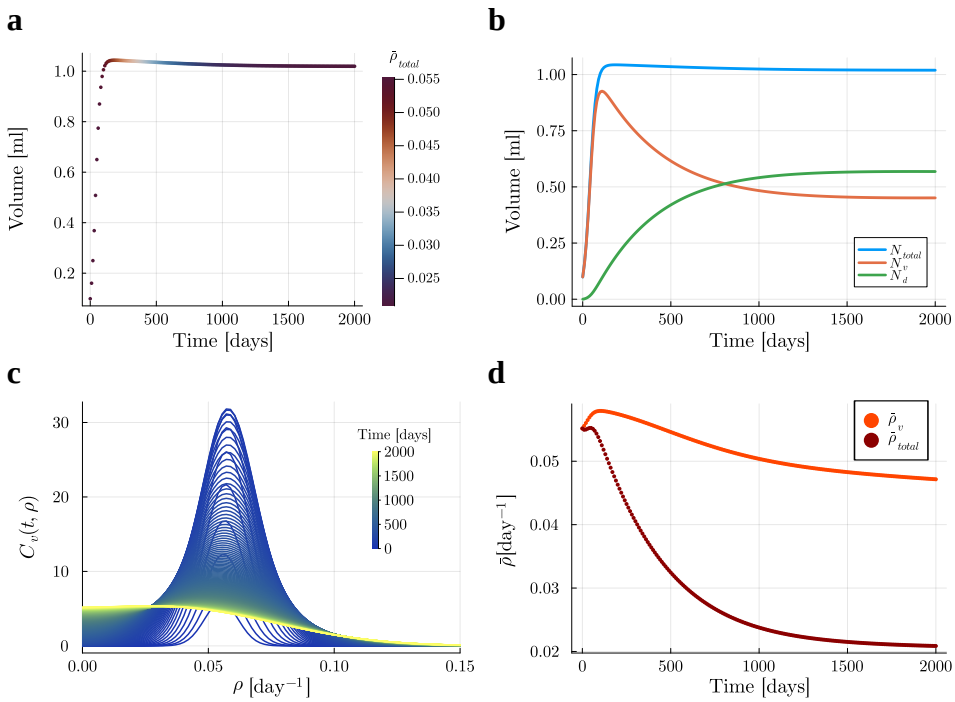

Fig. 2 Long-term model behavior for a tumor with the parameters $K = 1.05$ [ml] $s = 1.371$, $k_d = 0.74$ [day$^{(1-s)}$], $k_{cl} = 0.001$ [day^{-1}], $D = 4.87e-7$ [day^{-3}], $\sigma_0 = 0.00662$ [day^{-1}] for a time period of 2000 days. **(a)** Tumor volume trajectories: PDE solutions for the total tumor volume $N_{total}(t)$ (colored dots, hue scaled by population-wide mean proliferation rate $\bar{\rho}_{total}$). **(b)** Trajectories of the total tumor volume N_{total} (blue curve), the volume of the viable subpopulation N_v (orange curve), and the volume of the doomed subpopulation N_d (green curve). **(c)** Phenotypic restructuring: Viable cell distributions $C_v(t,\rho)$ from $t_0 = 0$ days (dark blue) to $t_{end} = 2000$ days (yellow). **(d)** Proliferation rate evolution: Temporal dynamics of $\bar{\rho}_{total}$ (entire population, red) and $\bar{\rho}_v$ (viable subpopulation, orange).

proliferation rate $\bar{\rho}_{total,0} = 0.05516$ [day^{-1}] (dark blue) broadens during early growth, then flattens and skews toward lower proliferation rates as the tumor stabilizes. This shift arises from two key processes: diffusion spreads the distribution and intrinsic mortality selectively removes cells with high proliferation rates. The resulting decline in population-wide mean proliferation rate $\bar{\rho}_{total}$ (red, Figure 2d) mirrors the phenotypic shift—initially rising during growth, then falling to a steady state of 0.02 [day^{-1}]. The viable subpopulation's mean proliferation rate $\bar{\rho}_v$ (orange) follows a similar trajectory of initial increase followed by a monotonic reduction, confirming that phenotypic selection occurs within the viable compartment.

Life-history trade-off as evolutionary constraint

To characterize the long-term evolutionary behavior of the proliferation-structured system, we employ the adaptive dynamics formalism to analyze the state-dependent

selection gradient and identify evolutionarily singular strategies. In particular, we examine how the proliferation–mortality trade-off term $k_d\rho^s$ constrains and shapes the selection of optimal proliferative phenotypes. For the proposed trade-off function, any $s > 0$ yields a monotonically increasing mortality rate with respect to ρ. When $s > 1$, the trade-off term is convex (Figure 3a, dark blue curve): mortality increases more than proportionally at high proliferation rates. This generates a steep negative selection gradient at large ρ and thereby imposes strong evolutionary constraints on further increases in proliferation. For $s = 1$, mortality increases proportionally with proliferation (Figure 3a, mid blue curve), implying a constant selection gradient. For $0 < s < 1$ (Figure 3a, light blue curve), mortality increases sublinearly with the proliferation rate, thereby reducing the incremental penalty for higher proliferation. $s = 0$ represents a simple logistic model with a constant intrinsic death rate, without trade-off.

This trade-off, counteracting the fitness gain by direct proliferative capacity, reshapes phenotypic fitness, as represented in the net growth rate $g(\rho)$ which defines a phenotype-dependent fitness landscape governing evolutionary dynamics:

$$g(\rho, N) = \underbrace{\rho\left(1 - \frac{N}{K}\right)}_{\text{Growth potential}} - \underbrace{k_d\rho^s}_{\text{Survival cost}} . \tag{2}$$

Depending on the value of s, this function produces distinct fitness landscapes. An interior fitness maximum exists only for $s > 1$, for which the net growth rate is strictly concave in ρ. This concavity condition ($\partial^2 g/\partial\rho^2 < 0$) arises because $\partial^2 g/\partial\rho^2 = -k_d s(s-1)\rho^{s-2}$ is strictly negative when $s > 1$. When $s \leq 1$, no interior maximum fitness exists. At $s = 1$, the second derivative vanishes, while for $s < 1$ it becomes positive, yielding a minimum, forcing the fitness optimum to the boundaries.
To derive the optimal evolutionary strategy ,ρ^*, we set the first derivative of $g(\rho, N)$ equal to 0, that gives:

$$\rho^* = \left(\frac{1 - N/K}{k_d s}\right)^{\frac{1}{s-1}} \tag{3}$$

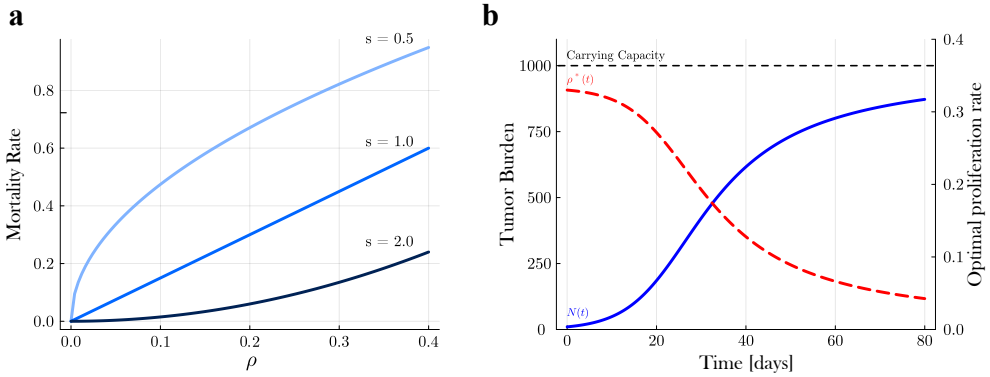

Fig. 3 Evolutionarily analysis of tumor growth dynamics **(a)** Mortality rate $k_d\rho^s$ as a function of proliferation rate ρ for trade-off steepness parameters $s = 0.5$ (light blue curve), $s = 1$ (mid blue curve), and $s = 2$ (dark blue curve), for $k_d = 1.5$. **(b)** Tumor burden for an exemplary tumor with the parameters $N_0 = 10\,\mathrm{mm}^3$, $K = 1000\,\mathrm{mm}^3$, $k_d = 1.5$ days, and $s = 2.0$. Tumor burden $N(t)$ (blue curve) increases logistically towards carrying capacity K (black dashed line). The maximum proliferation rate ρ^* (red curve) dynamcially decreases as tumor volumes approaches carrying capacity.

The net growth rate $g(\rho)$ and its maximizing trait, ρ^*, are dynamically coupled to tumor volume $N(t)$. This is an example of an eco-evolutionary dynamics, in which the environment is shaped by the strategies of all individuals, which in turn changes the optimal evolutionary strategy dynamically. For $s > 1$, as $N(t)$ (Figure 3b, blue curve) approaches the carrying capacity K, the growth potential term $\rho\left(1 - \frac{N}{K}\right)$ is progressively suppressed, leading to a decrease of ρ^* (red dashed curve) with $\lim_{N\to K} \rho^* = 0$. In this ecologically stable state, selection favors vanishing proliferation due to complete resource saturation. In this limit, our PDE with the diffusion term, keeps the system in a selection-mutation balance, where the population maintains a low but non-zero proliferation rate. For $s < 1$, by contrast, $\lim_{N\to K} \rho^* = \infty$, implying that, under any biologically constrained proliferation interval, the evolutionary attractor is driven toward the upper boundary of the admissible trait space. Such behavior corresponds to runaway selection for maximal proliferation and is therefore not biologically plausible. Consequently, we restrict our analysis to trade-off exponents $s > 1$. Further details on the dynamic reshaping of the fitness landscape, including the evolution of the net growth rate $g(\rho, N)$ are provided in the supplementary material (Section S5).

Treatment-driven selective pressures reshape tumor phenotypic landscapes

With experimental validation of our PDE framework's tumor growth simulations, we now investigate how cancer therapies reshape tumor dynamics through selective pressures. To model therapeutic interventions, we extend the system by adding a treatment term $-f(\rho) \cdot C_v(t, \rho)$ to the original equations, where $f(\rho)$ represents the proliferation-dependent killing rate. The extended model becomes:

$$\frac{\partial C_v(t,\rho)}{\partial t} = \underbrace{D\,\frac{\partial^2 C_v(t,\rho)}{\partial \rho^2}}_{\text{Diffusion}} + \underbrace{\rho\, C_v(t,\rho)\,(1-\frac{N(t)}{K})}_{\text{Logistic growth}} - \underbrace{k_d\,\rho^s\, C_v(t,\rho)}_{\text{Intrinsic death}} - \underbrace{f(\rho)\, C_v(t,\rho)}_{\text{Therapy death}} \quad (4a)$$

$$\frac{\partial C_d(t,\rho)}{\partial t} = k_d\,\rho^s\, C_v(t,\rho) + f(\rho)\, C_v(t,\rho) - \underbrace{k_{cl}\, C_d(t,\rho)}_{\text{Clearance}} \quad (4b)$$

Through *in silico* experiments, conducted without additional parameter fitting, we simulate four mechanistically distinct regimens applied as 10-day continuous treatments initiated at day 5. By comparing responses across targeting strategies, we identify how treatment-driven selection modulates the fitness trade-offs inherent in heterogeneous tumors. The areas under the curve of each treatment profile are normalized to enable comparative analysis of targeting strategy rather than dose intensity.

Pan-proliferation targeting

Cells are affected independently of their proliferation rate ρ, implementing uniform suppression across the phenotypic spectrum. The constant treatment effect follows $f_{uniform}(\rho) = k$, where k is a constant value applied identically to all proliferation rates (blue horizontal line in Figure 4a).

Low-proliferation targeting

Cells with low proliferation rates experience maximal suppression, with efficacy decreasing exponentially as ρ increases. This selective pressure follows $f_{low}(\rho) = ke^{-\lambda\rho}$, where λ controls the decay rate of treatment efficacy along the proliferation axis (orange curve in Figure 4a).

Mid-proliferation targeting

Maximal suppression targets cells with intermediate proliferation rates via a Gaussian profile centered at the population's initial mean proliferation rate $\bar{\rho}_0$. The treatment effect follows $f_{mid}(\rho) = exp\left(\frac{-(\rho-\bar{\rho}_0)^2}{2\sigma^2}\right)$ where σ determines the therapeutic breadth around the mean (purple curve in Figure 4a).

High-proliferation targeting

Cells with high proliferation rates are preferentially eliminated through an exponentially increasing treatment effect. The suppression profile is defined by $f_{high}(\rho) = ke^{\lambda\rho}$ where λ controls the growth rate of treatment efficacy (green curve in Figure 4a).

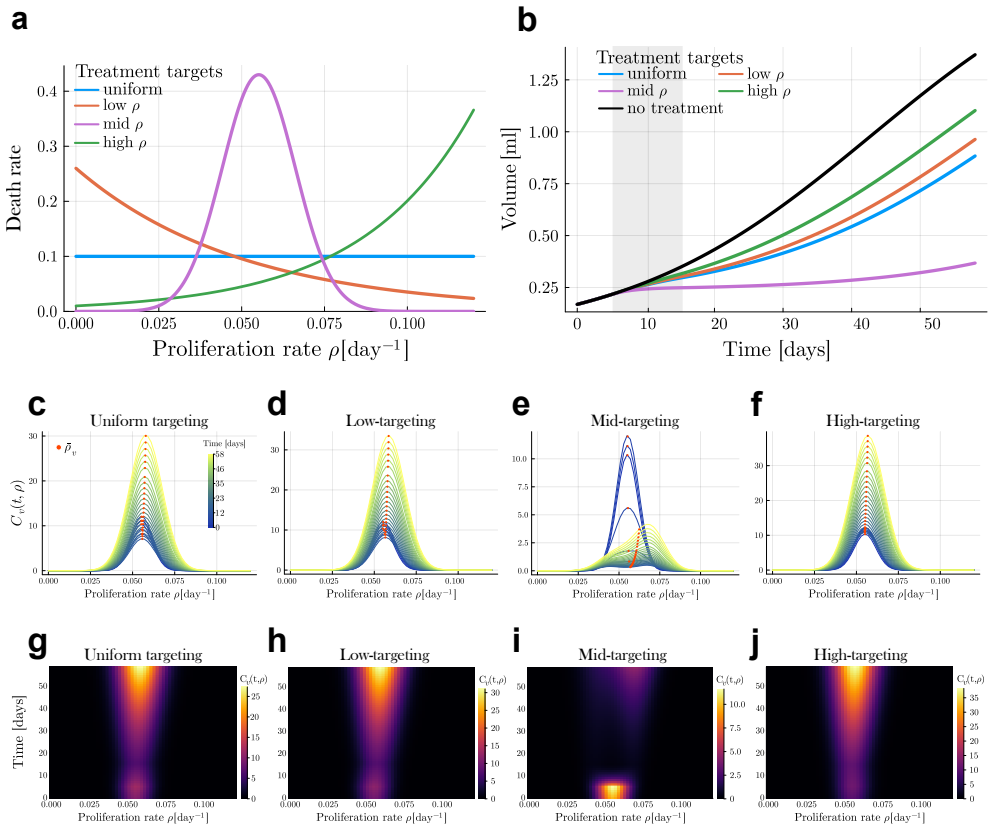

Fig. 4 Treatment-induced restructuring of phenotypic landscapes. **(a)** Therapeutic targeting profiles: Suppression functions for uniform (blue), slow-proliferation-targeted (orange), mid-proliferation-targeted (purple), and high-proliferation-targeted (green) regimens. **(b)** Tumor volumes following uniform-targeting (blue curve), low-proliferation targeted (orange curve), mid-proliferation targeted (purple curve), and high-proliferation targeted (green curve) regimes versus untreated control (black curve). All treatments were administered continuously from day 5 to day 15 (gray shaded regions). **(c-f)** Phenotypic shifts under treatment: Density plots of $C_v(t, \rho)$ for (b) uniform, (c) slow-targeting, (d) mid-targeting, and (e) high-targeting interventions., **(g-j)** Phenotypic shifts under treatment: Heatmaps of $C_v(t, \rho)$ for (g) uniform, (h) slow-targeting, (i) mid-targeting, and (j) high-targeting interventions. The proliferation rate ρ is shown on the x-axis, time in days is shown on the y-axis. Density is encoded from black (low density) to yellow (high density).

As expected, all treatment modalities reduced overall tumor burden relative to the untreated control (Figure 4b). However significant differences are observed in the primary clinical endpoints, as well as the phenotypic structure of the tumor.

Interestingly, this proliferation-structured model reproduces a characteristic feature of cytotoxic therapies such as chemotherapy and radiotherapy: tumor growth delay, a prolonged phase of growth suppression following the treatment window, before tumor regrowth resumes (Demidenko 2010; Yarnold et al. 1986). In classical unstructured growth models, this behavior typically requires the introduction of additional

delay terms or compartments (e.g., quiescent or senescent cell states). In contrast, within our PDE framework, this phenomenon emerges naturally from the adaptive reshaping of the proliferation-rate distribution during and after treatment. Among all treatment strategies considered, selective targeting of intermediate proliferation phenotypes yields the greatest reduction in tumor burden and maximally prolongs the time to relapse (Figure 4b).

The temporal evolution of tumor structure under different treatment modalities was characterized by shifts in cell density across proliferation rates, as shown in Figure 4c-j. Density plots (Figure 4c-f) with time encoded in a color scale from blue ($t = 0$) to yellow ($t = 58$), and heatmaps (Figure 4g-j), with the proliferation rate on the x-axis, time on the y-axis, and density encoded in a color scale from black (low density) to yellow (high density), revealed progressive restructuring of phenotypic distributions, collectively depicting the temporal evolution of tumor cell dynamics under different treatment modalities.

Next to the inhibited growth during treatment, all treatments also changed the population composition with each treatment strategy inducing distinct compositional shifts (Figure 4c-f). Uniform targeting resulted in the elimination of cells across all phenotypes, leading to a decrease in density throughout the proliferation-rate spectrum, narrowing the distribution compared to the pre-treatment condition (Figure 4c,g). In contrast, slow-proliferation-targeted treatment caused a reduction in density within the low-proliferation-rate region, selecting for cells with higher proliferation rates and creating a noticeable shift to the right side of the proliferation rate distribution (Figure 4d,h). When targeting intermediate proliferation rates, the treatment gave rise to a bimodal distribution, where slow- and fast-proliferating subpopulations coexisted, with very low densities in the mid-range (Figure 4e,i), signature of an evolutionary branching process. Finally, targeting high-proliferation-rate cells, a strategy that modulates the proliferation-mortality trade-off, led to a shift of the population toward lower proliferation rates during treatment (Figure 4f,j).

These phenotypic shifts are reflected in the dynamics of the mean proliferation rate. During the 10-day therapeutic window, all regimens drove a pronounced decline in $\bar{\rho}_{total}$ (Figure 5a), with the most substantial reduction observed under the mid-ρ-targeting treatment regime (purple points). Notably, post treatment, the mean proliferation rate rebounded across all groups, ultimately approaching pre-treatment baselines all regimes, but with substantial delay. The population-wide mean proliferation rate $\bar{\rho}_{total}$ declined during treatment, including in slow-proliferation-targeted regimens. The decrease in $\bar{\rho}_{total}$ in the slow-proliferation targeting treatment arose from the expanding doomed cell pool without proliferative capacity, reducing the population average.

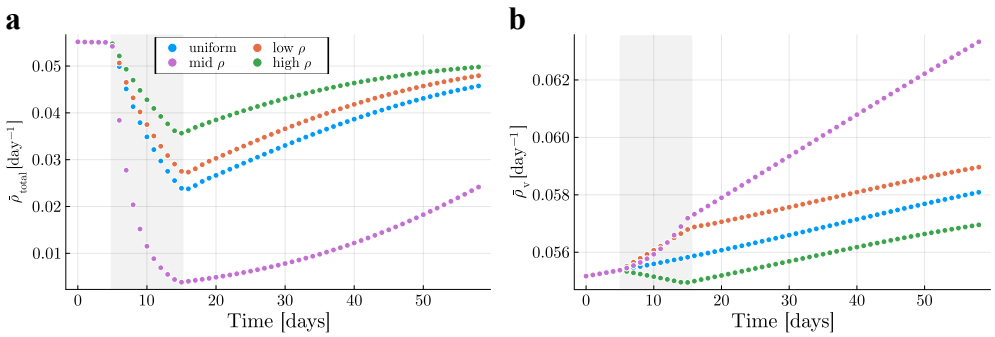

Fig. 5 Divergent proliferation dynamics and fitness landscape remodeling across therapeutic regimens. **(a)** Population-wide mean proliferation rate $\bar{\rho}_{total}(t)$. All regimens reduced $\bar{\rho}_{total}$ during treatment (days 5-15, gray shading), with mid-proliferation-targeted therapy (purple) showing the most pronounced decline. **(b)** Viable subpopulation mean proliferation rate $\bar{\rho}_v(t)$. Uniform (blue), slow-targeted (orange), and mid-targeted (purple) regimens increased $\bar{\rho}_v$ during treatment through selective elimination of slower-proliferating phenotypes, while high-targeted therapy (green) decreased $\bar{\rho}_v$ by preferentially eliminating fast-proliferating clones. All groups exhibited post-treatment increase in proliferation rates.

When examining viable cells exclusively (Figure 5b), all treatment strategies except the high-targeting regime (green) led to an increase in $\bar{\rho}_v$. Under the uniform-targeting treatment (blue), $\bar{\rho}_v$ increased during the treatment period and after the end of the treatment. Targeting low proliferation led to an increase in proliferation rates during treatment (orange). After the treatment period, the growth of $\bar{\rho}_v$ slowed down down (shoulder at day 15). A similar pattern can be observed under the mid-proliferation targeting regimen. During treatment, the increase in $\bar{\rho}_v$ under the mid-proliferation targeting regimen starts slower than under the low-proliferation targeting treatment. In the second half of the treatment period, the increase of $\bar{\rho}_v$ in the mid-proliferation targeting surpasses that of the low-proliferation targeting treatment. After treatment, $\bar{\rho}_v$ increases at similar rates in the uniform- and low-proliferation targeting, while it increases faster under the mid-proliferation treatment. Under the high-proliferation targeting treatment the $\bar{\rho}_v$ decreases during treatment since the treatment selects for slower proliferating cells (green). After the end of the treatment period, $\bar{\rho}_v$ in the high-proliferation targeting treatment increases at a similar rate as in the uniform and low-ρ targeting treatments.

3.1 Trade-off structure shapes proliferation distributions and dynamics

The monotonically increasing trade-off term (Equation (1a)) penalizes fast-growing cells exclusively, whereas the u-shaped trade-off term (Equation S.29) imposes a symmetric penalty on both very fast- and slow-growing cells. This difference in penalty structure directly shapes the model dynamics. In the absence of treatment, the u-shaped trade-off inherently favors intermediate proliferation rates, resulting in a

narrower initial proliferation rate distribution compared with the broader distribution observed under the monotonically increasing trade-off. Steady states in N_{total}, N_v, and N_d are reached more rapidly with the u-shaped trade-off, reducing the time required for phenotypic restructuring.

The resulting steady-state distributions also differ. Under the monotonically increasing trade-off, the distribution becomes flattened and skewed toward lower proliferation rates, whereas the u-shaped trade-off produces a more symmetric distribution with a high density around intermediate rates. These differences in final population composition directly reflect the distinct selective pressures imposed by the two trade-off mechanisms. Despite these microscopic differences, both trade-offs produce similar tumor growth curves.

Under treatment, the behaviors of the two models are largely comparable. In both cases, the population-wide mean proliferation rate $\bar{\rho}_{total}$ decreases during treatment and increases again afterward. With the u-shaped trade-off, $\bar{\rho}_{total}$ returns to its initial value within the simulated period of 58 days, whereas it remains below the initial value when the monotonically increasing trade-off is used. This difference reflects the faster convergence to steady state under the u-shaped trade-off. The viable population's mean proliferation rate, $\bar{\rho}_v$, shows similar trends under both trade-offs: it increases during treatment for the uniform, low-targeting, and mid-targeting treatments, but decreases under the high-targeting treatment.

4 Discussion

Our phenotype-structured PDE model reveals that intra-tumor heterogeneity in proliferation rate, driven by phenotypic diffusion and shaped by life-history trade-offs, fundamentally governs tumor growth dynamics and evolutionary trajectories. Model calibration to longitudinal data confirms that the trade-off is essential for accurate tumor volume prediction. Furthermore, we demonstrate that the maximum fitness strategy for proliferation rate dynamically declines as tumors grow, reflecting a shift toward slower, more resource-efficient phenotypes under increasing competition. In silico treatment experiments reveal that targeting different regions of the proliferation spectrum induces distinct phenotypic restructurings: high-proliferation targeting suppresses fast growers, while low- or mid-range targeting can enrich aggressive clones, highlighting how therapy can reshape fitness landscapes and influence resistance evolution.

A critical distinction from classical reaction-diffusion frameworks (e.g., Fisher-KPP equations) lies in our implementation of growth regulation. While Fisher-KPP systems typically employ *local* density dependence that supports traveling waves, our model imposes *global* resource competition through the logistic term where $N(t)$ integrates all phenotypes. This global coupling enforces uniform nutrient constraints across the proliferation spectrum, reflecting the systemic resource limitations observed in solid tumors. Regarding phenotypic diffusion, we maintain a density-independent formulation. While density-dependent diffusion terms have been proposed in other contexts such as tumor invasion (Tao and Tello 2015) and glioblastoma growth (Stepien et al. 2015) to capture spatial constraints, in our model diffusion represents genetic drift

driven by stochastic mutations. Adopting density-dependent diffusion would imply that mutation rates scale with tumor size, a biologically unsupported premise.

Our model complements and extends existing frameworks for understanding treatment-induced evolution in cancer. Our model synergizes with the second-strike framework proposed by Gatenby et al. (2020), which proposes that tumors treated with a first treatment which reduces both tumor volume and ITH, become vulnerable to elimination by a second strike. While their model identifies the opportunity for extinction via first-strike-second-strike treatment, our framework provides the phenotypic roadmap: it predicts both the dominant traits and evolving heterogeneity patterns within the residual viable population after the first treatment. By predicting how heterogeneity shifts during treatment, we can select the second strike tailored to target the emergent phenotypic landscape. Thus, our contribution lies in offering a computational platform to identify and schedule synergistic treatment pairs where the first strike achieves sufficient volume reduction and the second strike selectively eliminates the resistant phenotype. Furthermore, our results align with findings from compartmental ODE models of proliferation heterogeneity, which have shown that targeting high-proliferation subpopulations can effectively suppress tumor growth and alter post-treatment regrowth dynamics by selecting for slower proliferating cells (Raatz et al. 2021). Incorporating heterogeneity in reproductive capacity as a continuously evolving trait in a PDE model enabled a systematic investigation of different treatment modalities and facilitates the application of adaptive dynamics principles with a classical tumor growth model, explaining the emergence of dominant clones and predicting how their fitness changes over time and in response to therapy. Together, the synergies between our framework and existing modeling approaches position our model as a tool for predicting relapse dynamics and designing combinatorial strategies that exploit the evolutionary trajectory of the tumor, moving beyond monomorphic or compartmental models toward a dynamic, predictive understanding of cancer evolution.

While our phenotype-structured PDE framework provides a powerful mechanistic description of proliferation-driven tumor dynamics, several aspects offer opportunities for future improvement. The model assumes a well-mixed, non-spatial tumor environment and does not explicitly account for spatial heterogeneity, such as nutrient gradients or physical barriers, which can strongly influence local selection pressures and clonal competition in solid tumors. We focus on proliferation rate as a single, isolated trait, whereas in reality, phenotypic evolution involves trade-offs with other key traits such as migration, metabolism, or therapy resistance, which could be integrated to capture more complex adaptive strategies. Although our model accurately predicts macroscopic tumor growth, its predictions about the compositional shifts in phenotypic subpopulations—while mechanistically plausible—remain unvalidated due to limitations in longitudinal *in vivo* monitoring of phenotype distributions. Parameterization relies on fitting to bulk volume data and assumptions about initial phenotypic variance and trade-off structure, highlighting the need for more granular single-cell or lineage-tracing data to refine these estimates. Future work will extend the model to incorporate treatment data from clinical or preclinical trials, enabling direct comparison with observed resistance patterns. Moreover, for highly heterogeneous or spatially

structured tumors, the PDE framework may be complemented by agent-based or hybrid models to capture emergent spatial and stochastic dynamics.

References

(2026) SciML/MethodOfLines.jl. SciML Open Source Scientific Machine Learning

Aktipis CA, Boddy AM, Gatenby RA, et al (2013) Life history trade-offs in cancer evolution. Nat Rev Cancer 13(12):883–892. https://doi.org/10.1038/nrc3606

Bezanson J, Edelman A, Karpinski S, et al (2017) Julia: A fresh approach to numerical computing. SIAM Review 59(1):65–98. https://doi.org/10.1137/141000671

Boddy AM, Huang W, Aktipis A (2018) Life History Trade-Offs in Tumors. Curr Pathobiol Rep 6(4):201–207. https://doi.org/10.1007/s40139-018-0188-4

Brännström Å, Johansson J, Festenberg NV (2013) The Hitchhiker's Guide to Adaptive Dynamics. Games 4(3):304–328. https://doi.org/10.3390/g4030304

Caswell DR, Swanton C (2017) The role of tumour heterogeneity and clonal cooperativity in metastasis, immune evasion and clinical outcome. BMC Med 15(1):133. https://doi.org/10.1186/s12916-017-0900-y

Cho H, Levy D (2018) Modeling the chemotherapy-induced selection of drug-resistant traits during tumor growth. Journal of Theoretical Biology 436:120–134. https://doi.org/10.1016/j.jtbi.2017.10.005

de Visser JAGM, Krug J (2014) Empirical fitness landscapes and the predictability of evolution. Nat Rev Genet 15(7):480–490. https://doi.org/10.1038/nrg3744

Demidenko E (2010) Three endpoints of in vivo tumour radiobiology and their statistical estimation. Int J Radiat Biol 86(2):164–173. https://doi.org/10.3109/09553000903419304

Dieckmann U, Law R (1996) The dynamical theory of coevolution: A derivation from stochastic ecological processes. J Math Biology 34(5-6):579–612. https://doi.org/10.1007/BF02409751

Dierckx P (2023) Curve and Surface Fitting with Splines. Oxford Scholarship Online, Clarendon, Oxford, https://doi.org/10.1093/oso/9780198534419.001.0001

Durrett R, Foo J, Leder K, et al (2011) Intratumor Heterogeneity in Evolutionary Models of Tumor Progression. Genetics 188(2):461–477. https://doi.org/10.1534/genetics.110.125724

Ekkers DM, Tusso S, Moreno-Gamez S, et al (2022) Trade-Offs Predicted by Metabolic Network Structure Give Rise to Evolutionary Specialization and Phenotypic Diversification. Mol Biol Evol 39(6)

Farahpour F, Saeedghalati M, Brauer VS, et al (2018) Trade-off shapes diversity in eco-evolutionary dynamics. elife 7:e36273

Fiandaca G, Bernardi S, Scianna M, et al (2022) A phenotype-structured model to reproduce the avascular growth of a tumor and its interaction with the surrounding environment. Journal of Theoretical Biology 535:110980. https://doi.org/10.1016/j.jtbi.2021.110980

Gallaher JA, Brown JS, Anderson ARA (2019) The impact of proliferation-migration tradeoffs on phenotypic evolution in cancer. Sci Rep 9(1):2425. https://doi.org/10.1038/s41598-019-39636-x

Ganeshan K, Nikkanen J, Man K, et al (2019) Energetic Trade-Offs and Hypometabolic States Promote Disease Tolerance. Cell 177(2):399–413.e12. https://doi.org/10.1016/j.cell.2019.01.050

Gatenby RA, Artzy-Randrup Y, Epstein T, et al (2020) Eradicating Metastatic Cancer and the Eco-Evolutionary Dynamics of Anthropocene Extinctions. Cancer Res 80(3):613–623. https://doi.org/10.1158/0008-5472.CAN-19-1941

Ghalambor CK, Martin TE (2001) Fecundity-survival trade-offs and parental risk-taking in birds. Science 292(5516):494–497. https://doi.org/10.1126/science.1059379

Heppner GH (1984) Tumor heterogeneity. Cancer Res 44(6):2259–2265

Herren CM, Baym M (2022) Decreased thermal niche breadth as a trade-off of antibiotic resistance. ISME J 16(7):1843–1852. https://doi.org/10.1038/s41396-022-01235-6

Kim D, Hwang CY, Cho KH (2024) The fitness trade-off between growth and stress resistance determines the phenotypic landscape. BMC Biol 22(1):62. https://doi.org/10.1186/s12915-024-01856-7

King T, Ishihama A, Kori A, et al (2004) A Regulatory Trade-Off as a Source of Strain Variation in the Species Escherichia coli. Journal of Bacteriology 186(17):5614–5620. https://doi.org/10.1128/jb.186.17.5614-5620.2004

Kondo H, Ratcliffe CDH, Hooper S, et al (2021) Single-cell resolved imaging reveals intra-tumor heterogeneity in glycolysis, transitions between metabolic states, and their regulatory mechanisms. Cell Reports 34(7):108750. https://doi.org/10.1016/j.celrep.2021.108750

Lemaître JF, Berger V, Bonenfant C, et al (2015) Early-late life trade-offs and the evolution of ageing in the wild. Proc Biol Sci 282(1806):20150209. https://doi.org/10.1098/rspb.2015.0209

Lorenzi T, Chisholm RH, Clairambault J (2016) Tracking the evolution of cancer cell populations through the mathematical lens of phenotype-structured equations. Biol Direct 11(1):43. https://doi.org/10.1186/s13062-016-0143-4

Lu C, Brauer MJ, Botstein D (2009) Slow Growth Induces Heat-Shock Resistance in Normal and Respiratory-deficient Yeast. MBoC 20(3):891–903. https://doi.org/10.1091/mbc.e08-08-0852

Lucas O, Ward S, Zaidi R, et al (2025) Characterizing the evolutionary dynamics of cancer proliferation in single-cell clones with SPRINTER. Nat Genet 57(1):103–114. https://doi.org/10.1038/s41588-024-01989-z

Ma Y, Gowda S, Anantharaman R, et al (2022) ModelingToolkit: A Composable Graph Transformation System For Equation-Based Modeling. https://doi.org/10.48550/arXiv.2103.05244, arXiv:2103.05244

Macal C, North M (2005) Tutorial on agent-based modeling and simulation. In: Proceedings of the Winter Simulation Conference, 2005., pp 14 pp.–, https://doi.org/10.1109/WSC.2005.1574234

Maley CC, Aktipis A, Graham TA, et al (2017) Classifying the evolutionary and ecological features of neoplasms. Nat Rev Cancer 17(10):605–619. https://doi.org/10.1038/nrc.2017.69

Marusyk A, Janiszewska M, Polyak K (2020) Intratumor Heterogeneity: The Rosetta Stone of Therapy Resistance. Cancer Cell 37(4):471–484. https://doi.org/10.1016/j.ccell.2020.03.007

McDade TW, Georgiev AV, Kuzawa CW (2016) Trade-offs between acquired and innate immune defenses in humans. Evol Med Public Health 2016(1)

Meng X, Zheng Y, Zhang L, et al (2024) Single-Cell Analyses Reveal the Metabolic Heterogeneity and Plasticity of the Tumor Microenvironment during Head and Neck Squamous Cell Carcinoma Progression. Cancer Res 84(15):2468–2483. https://doi.org/10.1158/0008-5472.CAN-23-1344

Partridge L, Gems D, Withers DJ (2005) Sex and death: What is the connection? Cell 120(4):461–472. https://doi.org/10.1016/j.cell.2005.01.026

Phan K, Ferenci T (2013) A design-constraint trade-off underpins the diversity in ecologically important traits in species Escherichia coli. ISME J 7(10):2034–2043. https://doi.org/10.1038/ismej.2013.82

Raatz M, Shah S, Chitadze G, et al (2021) The impact of phenotypic heterogeneity of tumour cells on treatment and relapse dynamics. PLoS Computational Biology 17(2):e1008702

Rackauckas C, Nie Q (2017) Differentialequations.jl – a performant and feature-rich ecosystem for solving differential equations in julia. The Journal of Open Research Software 5(1). https://doi.org/10.5334/jors.151, URL https://app.dimensions.ai/details/publication/pub.1085583166andhttp://openresearchsoftware.metajnl.com/articles/10.5334/jors.151/galley/245/download/, exported from https://app.dimensions.ai on 2019/05/05

Raj A, van Oudenaarden A (2008) Stochastic gene expression and its consequences. Cell 135(2):216–226. https://doi.org/10.1016/j.cell.2008.09.050

Richards EJ (2006) Inherited epigenetic variation — revisiting soft inheritance. Nat Rev Genet 7(5):395–401. https://doi.org/10.1038/nrg1834

Schlatter DC, Kinkel LL (2015) Do tradeoffs structure antibiotic inhibition, resistance, and resource use among soil-borne Streptomyces? BMC Evol Biol 15(1):186. https://doi.org/10.1186/s12862-015-0470-6

Schwenke RA, Lazzaro BP, Wolfner MF (2016) Reproduction–Immunity Trade-Offs in Insects. Annual Review of Entomology 61(Volume 61, 2016):239–256. https://doi.org/10.1146/annurev-ento-010715-023924

Shoval O, Sheftel H, Shinar G, et al (2012) Evolutionary Trade-Offs, Pareto Optimality, and the Geometry of Phenotype Space. Science 336(6085):1157–1160. https://doi.org/10.1126/science.1217405

Sobral D, Martins M, Kaplan S, et al (2022) Genetic and microenvironmental intra-tumor heterogeneity impacts colorectal cancer evolution and metastatic development. Commun Biol 5(1):937. https://doi.org/10.1038/s42003-022-03884-x

Stearns SC (1989) Trade-Offs in Life-History Evolution. Functional Ecology 3(3):259–268. https://doi.org/10.2307/2389364, 2389364

Stepien TL, Rutter EM, Kuang Y (2015) A data-motivated density-dependent diffusion model of in vitro glioblastoma growth. MBE 12(6):1157–1172. https://doi.org/10.3934/mbe.2015.12.1157

Tao Y, Tello JI (2015) Nonlinear stability of a heterogeneous state in a PDE-ODE model for acid-mediated tumor invasion. MBE 13(1):193–207. https://doi.org/10.3934/mbe.2016.13.193

Travers LM, Garcia-Gonzalez F, Simmons LW (2015) Live fast die young life history in females: Evolutionary trade-off between early life mating and lifespan in female Drosophila melanogaster. Sci Rep 5(1):15469. https://doi.org/10.1038/srep15469

Vitale I, Shema E, Loi S, et al (2021) Intratumoral heterogeneity in cancer progression and response to immunotherapy. Nat Med 27(2):212–224. https://doi.org/10.1038/s41591-021-01233-9

Wang Y, Zhou JX, Pedrini E, et al (2023) Cell Population Growth Kinetics in the Presence of Stochastic Heterogeneity of Cell Phenotype. Journal of Theoretical Biology 575:111645. https://doi.org/10.1016/j.jtbi.2023.111645, arXiv:2301.03782 [q-bio]

West J, Robertson-Tessi M, Anderson ARA (2023) Agent-based methods facilitate integrative science in cancer. Trends Cell Biol 33(4):300–311. https://doi.org/10.1016/j.tcb.2022.10.006

Wood KB, Cluzel P (2012) Trade-offs between drug toxicity and benefit in the multi-antibiotic resistance system underlie optimal growth of E. coli. BMC Syst Biol 6(1):48. https://doi.org/10.1186/1752-0509-6-48

Yarnold JR, Bamber JC, Gibbs J (1986) Tumour growth delay as a clinical endpoint for the measurement of radiation response. Radiotherapy and Oncology 5(3):207–214. https://doi.org/10.1016/S0167-8140(86)80050-0

Zakrzewska A, van Eikenhorst G, Burggraaff JEC, et al (2011) Genome-wide analysis of yeast stress survival and tolerance acquisition to analyze the central trade-off between growth rate and cellular robustness. MBoC 22(22):4435–4446. https://doi.org/10.1091/mbc.e10-08-0721

Zhang Y, Shi M, Li M, et al (2025) Dynamic single-cell metabolomics reveals cell-cell interaction between tumor cells and macrophages. Nat Commun 16(1):4582. https://doi.org/10.1038/s41467-025-59878-w

Zhao L, Chen H, Guo Z, et al (2020) Targeted radionuclide therapy in patient-derived xenografts using 177Lu-EB-RGD. Mol Cancer Ther 19(10):2034–2043. https://doi.org/10.1158/1535-7163.MCT-19-1098